HOS Simulations of Nonlinear Water Waves in Complex Media

Philippe Guyenne

Abstract We present an overview of recent extensions of the high-order spectral method of Craig and Sulem (J Comput Phys 108:73–83, 1993) to simulating nonlinear water waves in a complex environment. Under consideration are cases of wave propagation in the presence of fragmented sea ice, variable bathymetry and a vertically sheared current. Key components of this method, which apply to all three cases, include reduction of the full problem to a lower-dimensional system involving boundary variables alone, and a Taylor series representation of the Dirichlet–Neumann operator. This results in a very efficient and accurate numerical solver by using the fast Fourier transform. Two-dimensional simulations of unsteady wave phenomena are shown to illustrate the performance and versatility of this approach.

1 Introduction

The potential-flow formulation of Euler's equations for water waves has been very popular among both the mathematical and engineering communities, as it has proved to be successful at describing a wide range of wave phenomena. Via application of nonlocal operators, this formulation allows the original Laplace problem to be reduced from one posed inside the fluid domain to one posed on the boundary alone, thus allowing for dimensionality reduction. Moreover, in the absence of dissipative effects, the governing equations can be recast as a

P. Guyenne (✉)
Department of Mathematical Sciences, University of Delaware, Newark, DE, USA
e-mail: guyenne@udel.edu

canonical Hamiltonian system in terms of two conjugate variables, namely the surface elevation and the velocity potential evaluated there [40]. Due to these nice features, the potential-flow formulation has served as the theoretical basis in a countless number of water-wave studies, ranging from rigorous mathematical analysis to direct numerical simulation and weakly nonlinear modeling in various asymptotic regimes.

One of the most popular choices for direct numerical simulation is the so-called high-order spectral (HOS) approach, which is based on a Taylor series expansion of the Dirichlet–Neumann operator (DNO) combined with a pseudospectral scheme for space discretization using the fast Fourier transform. This is a very efficient and accurate numerical method when it is applicable. Compared to boundary integral methods [17, 19], it provides a faster recursive procedure for solving Laplace's equation in an irregular domain that is a perturbation to a simple geometry. Its computer implementation is also relatively easy and insensitive to the spatial dimension of the problem. From a general perspective, the basic idea underlying this approach is not marginal at all and, to some extent, shares similarities with other "fast" algorithms that are nowadays popular in scientific computing. For example, the fast multipole method [16] and more recently the method of quadrature by expansion [1] or the fast Chebyshev–Legendre transform [26] all rely on some sort of approximate series expansion in order to speed up computations. For the interested reader, details on boundary integral methods and other techniques can be found in other papers of this special volume.

The HOS approach was first introduced by Dommermuth and Yue [13] and West et al. [38] to simulate nonlinear gravity waves on uniform depth. Since then, it has been extended and applied to wave phenomena in various settings by many other investigators [14, 15, 28]. Slightly later than [13, 38], Craig and Sulem [6] proposed a related numerical method that has also been used with success in a number of subsequent applications [7, 8, 10, 30]. In particular, results were validated via comparison with laboratory experiments, weakly nonlinear predictions or other numerical solvers [9, 21–23, 39]. While these two HOS approaches are similar in their derivation, implementation and performance, there is a fundamental difference in their definition of the DNO. Dommermuth and Yue [13] and West et al. [38] define their DNO in terms of the vertical fluid velocity at the free surface, while Craig and Sulem [6] define their DNO in terms of the normal fluid velocity. These are two different quantities for a nontrivial free surface. In the latter definition, the DNO can be shown to be analytic with respect to surface deformations, which gives a justification for its Taylor series representation and thus a rigorous mathematical foundation for the corresponding HOS method [3]. Another important property of the DNO in that definition is its self-adjointness, which results in efficient and relatively simple recursion formulas for its computation [5, 30].

In an effort to improve the convergence of the DNO series, Nicholls and Reitich [32, 33] developed variants of Craig and Sulem's approach, which they refer to as Field Expansion and Transformed Field Expansion algorithms. These however require a hodograph transformation to map the irregular physical domain to a regular computational domain, together with a full-dimensional solution, because

the elliptic problem becomes inhomogeneous. So far, they have only been used to compute traveling waves (i.e. steady waves in a moving reference frame) and to investigate the spectral stability of these solutions. A review on this body of work can be found in [31].

In this paper, we present an overview of recent work by the author and collaborators, that extends Craig and Sulem's approach to wave propagation in a complex environment. Most of these results have been obtained in the past decade or so, with a focus on unsteady solutions in the time domain. More specifically, we present direct numerical simulations of nonlinear dispersive waves in the presence of (i) fragmented sea ice [24], (ii) bottom topography [21] and (iii) a background shear current [18]. All three problems go beyond the classical setting of wave propagation in a homogeneous medium, and are of practical relevance to the fields of oceanography and coastal engineering. In particular, problem (i) has experienced renewed interest due to the rapid decline of summer ice extent that has occurred in the Arctic Ocean over recent years. Problem (iii) has also drawn much attention lately, especially from the mathematical community [4, 37], because it represents a refinement of the standard potential-flow formulation, allowing for rotational water waves. Therefore, we now find it timely to write a review paper on these recent advances, even more so considering that we are not aware of any previous review specifically on the HOS technique proposed by Craig and Sulem [6].

In all three cases, the numerical algorithm is based on the same original principle, and thus inherits the same qualities of accuracy and efficiency. In case (i), a mixed continuum-piecewise representation of flexural rigidity is adopted to specify an irregular array of ice floes on water. The main objective here is to emulate wave attenuation by scattering through an inhomogeneous ice field, as it may occur in the oceanic marginal ice zone. In contrast to linear predictions [36], slow or fast wave decay is observed depending on wave and ice parameters. In case (ii), the DNO exhibits an additional component that can be expanded in terms of bottom deformations. The inherent smoothing character of the DNO with respect to water depth is clearly revealed in this series expansion through the recurring presence of a smoothing Fourier multiplier. As a result, both smooth and non-smooth bottom profiles can be accommodated by this HOS method. In case (iii), wave propagation in the presence of constant nonzero vorticity is considered. This type of vorticity corresponds to a background shear current with a linear profile in the vertical direction. In addition to the DNO, another nonlocal operator (the Hilbert transform) is required in order to define a stream function at the free surface. A Taylor series expansion is also introduced for the fast computation of this operator. For an adverse current in deep water, it is confirmed that the Benjamin–Feir instability of Stokes waves may be significantly enhanced and may lead to the formation of large rogue waves [15].

The remainder of this paper is organized as follows. Sections 2 and 3 recall the basic governing equations in the potential-flow formulation for nonlinear water waves on uniform depth, as well as the corresponding Hamiltonian reduction and numerical discretization. While our HOS approach is extensible to three dimensions [5, 11, 25, 30, 39], we focus here on the two-dimensional case. Section 4 presents

numerical results for wave propagation in the three different settings mentioned above (fragmented sea ice, variable bottom and shear current), with each setting discussed separately. In each case, we highlight the main points in the extension of the classical formulation.

2 Mathematical Formulation

2.1 Governing Equations

We consider the motion of a free surface on top of a two-dimensional ideal fluid of uniform depth h. In Cartesian coordinates, the x-axis is the direction of wave propagation and the y-axis points upward. The free surface is assumed to be the graph of a function $y = \eta(x, t)$. For potential flow, the velocity field is given by $\mathbf{u} = (u, v)^\top = \nabla\varphi$ where $\varphi(x, y, t)$ denotes the velocity potential. In terms of these variables, the initial boundary value problem for irrotational water waves associated with the fluid domain

$$S(\eta) = \{x \in \mathbb{R}, -h < y < \eta(x, t)\},$$

can be stated as

$$\Delta\varphi = 0, \quad \text{in} \quad S(\eta), \tag{2.1}$$

$$\eta_t - \varphi_y + \varphi_x \eta_x = 0, \quad \text{at} \quad y = \eta(x, t), \tag{2.2}$$

$$\varphi_t + \frac{1}{2}(\varphi_x^2 + \varphi_y^2) + g\eta + P = 0, \quad \text{at} \quad y = \eta(x, t), \tag{2.3}$$

$$\varphi_y = 0, \quad \text{at} \quad y = -h, \tag{2.4}$$

where g is the acceleration due to gravity and P represents normal stresses acting on the free surface (here $P = 0$ except for the sea-ice case where it is meant to model the bending force exerted by the floating ice sheet). Note that subscripts are used as shorthand notation for partial or variational derivatives (i.e. $\varphi_t = \partial_t \varphi$).

Following [6, 40], the dimensionality of the Laplace problem (2.1)–(2.4) can be reduced by introducing the trace of the velocity potential on the free surface, $\xi(x, t) = \varphi(x, \eta(x, t), t)$ together with the Dirichlet–Neumann operator (DNO)

$$G(\eta) : \xi \longmapsto (-\eta_x, 1)^\top \cdot \nabla\varphi\big|_{y=\eta},$$

which is the singular integral operator that takes Dirichlet data ξ at $y = \eta(x, t)$, solves Laplace's equation (2.1) subject to (2.4), and returns the corresponding

Neumann data (i.e. the normal velocity at the free surface). If $P = 0$, the resulting equations can be expressed as a canonical Hamiltonian system

$$\begin{pmatrix} \eta_t \\ \xi_t \end{pmatrix} = \begin{pmatrix} 0 & 1 \\ -1 & 0 \end{pmatrix} \begin{pmatrix} H_\eta \\ H_\xi \end{pmatrix},$$

for the conjugate variables η and ξ, whose Hamiltonian

$$H = \frac{1}{2} \int_{-\infty}^{\infty} \left[\xi G(\eta)\xi + g\eta^2 \right] dx,$$

corresponds to the total energy that is conserved over time. These equations more explicitly read

$$\eta_t = G(\eta)\xi, \tag{2.5}$$

$$\xi_t = -g\eta - \frac{1}{2(1 + \eta_x^2)} \left[\xi_x^2 - (G(\eta)\xi)^2 - 2\xi_x \eta_x G(\eta)\xi \right]. \tag{2.6}$$

2.2 Dirichlet–Neumann Operator

Equations (2.5) and (2.6) form a closed system for the two unknowns η and ξ. The question now is how to determine $G(\eta)\xi$ given η and ξ at any time, so that the right-hand sides of (2.5) and (2.6) can be evaluated. In two dimensions, it is known that G is an analytic function of η if $\eta \in \text{Lip}(\mathbb{R})$ [3]. Consequently, for surface perturbations around the quiescent state $\eta = 0$, the DNO can be written in terms of a convergent Taylor series expansion

$$G(\eta) = \sum_{j=0}^{\infty} G_j(\eta), \tag{2.7}$$

where the Taylor polynomials G_j are homogeneous of degree j in η and, as shown in [5, 6], they can be determined recursively: for even $j > 0$,

$$G_j = G_0 D^{j-1} \frac{\eta^j}{j!} D - \sum_{\ell=2,\,\text{even}}^{j} D^\ell \frac{\eta^\ell}{\ell!} G_{j-\ell} - \sum_{\ell=1,\,\text{odd}}^{j-1} G_0 D^{\ell-1} \frac{\eta^\ell}{\ell!} G_{j-\ell}, \tag{2.8}$$

and, for odd j,

$$G_j = D^j \frac{\eta^j}{j!} D - \sum_{\ell=2,\,\text{even}}^{j-1} D^\ell \frac{\eta^\ell}{\ell!} G_{j-\ell} - \sum_{\ell=1,\,\text{odd}}^{j} G_0 D^{\ell-1} \frac{\eta^\ell}{\ell!} G_{j-\ell}, \tag{2.9}$$

where $D = -\mathrm{i}\partial_x$ and $G_0 = D\tanh(hD)$ are Fourier multiplier operators. In the infinite-depth limit ($h \to +\infty$), G_0 reduces to $|D|$ but otherwise Eqs. (2.8) and (2.9) remain unchanged. Using (2.7) together with (2.8) and (2.9) requires that η be a smooth single-valued function of x and thus overturning waves with a multivalued profile are not permitted. These formulas provide an efficient and accurate Laplace solver that lies at the heart of our HOS scheme as outlined below.

3 Numerical Methods

3.1 Space Discretization

Assuming periodic boundary conditions in the periodic cell $x \in [0, L_m)$, we use a pseudo-spectral method based on the fast Fourier transform (FFT). This is a suitable choice for computing the DNO since each term in (2.7) consists of concatenations of Fourier multipliers with powers of η. Accordingly, both functions η and ξ are expanded in truncated Fourier series

$$\begin{pmatrix} \eta \\ \xi \end{pmatrix} = \sum_{k=-k_m}^{k_m} \begin{pmatrix} \widehat{\eta}_k \\ \widehat{\xi}_k \end{pmatrix} e^{\mathrm{i}kx}.$$

The spatial derivatives and Fourier multipliers are evaluated in the Fourier space, while the nonlinear products are calculated in the physical space on a regular grid of N collocation points. For example, if we wish to apply the zeroth-order operator G_0 to a function ξ in the physical space, we first transform ξ to the Fourier space, apply the diagonal operator $k\tanh(hk)$ to the Fourier coefficients $\widehat{\xi}_k$ and then transform back to the physical space.

In practice, the DNO series (2.7) is also truncated to a finite number of terms M but, by analyticity, a small number of terms (typically $M < 10 \ll N$) is sufficient to achieve highly accurate results [30, 32, 39]. Note that formulas (2.8) and (2.9) are slightly different from those originally given in [6] regarding the order of application of the various operators. As pointed out in [5], the DNO is self-adjoint and therefore the adjoint formulas (2.8) and (2.9) are equivalent to the original ones. This property however has important consequences on the DNO implementation and on the computational efficiency of the HOS approach. These adjoint formulas allow us to store and reuse the G_j's as vector operations on ξ, instead of having to recompute them at each order when applied to concatenations of Fourier multipliers and powers of η. This results in faster calculations and the computational cost for evaluating (2.7) is estimated to be $O(M^2 N \log N)$ operations via the FFT. Aliasing errors are removed by zero-padding in the Fourier space [30].

3.2 Time Integration

Time integration of (2.5) and (2.6) is performed in the Fourier space, which is advantageous for two main reasons. First, solving the time evolution problem amounts to solving an ODE system for the Fourier coefficients $\widehat{\eta}_k$ and $\widehat{\xi}_k$ rather than a PDE system for η and ξ. As mentioned above, the spatial derivatives are computed with spectral accuracy via the FFT. Second, the linear terms can be solved exactly by the integrating factor technique [6, 22, 39].

For this purpose, we separate the linear and nonlinear parts in (2.5) and (2.6). Setting $\mathbf{v} = (\eta, \xi)^\top$, these equations can be expressed as

$$\partial_t \mathbf{v} = \mathcal{L}\mathbf{v} + \mathcal{N}(\mathbf{v}), \tag{3.1}$$

where the linear part $\mathcal{L}\mathbf{v}$ is defined by

$$\mathcal{L}\mathbf{v} = \begin{pmatrix} 0 & G_0 \\ -g & 0 \end{pmatrix} \begin{pmatrix} \eta \\ \xi \end{pmatrix},$$

and the nonlinear part $\mathcal{N}(\mathbf{v})$ is given by

$$\mathcal{N}(\mathbf{v}) = \begin{pmatrix} \big[G(\eta) - G_0\big]\xi \\ -\frac{1}{2(1+\eta_x^2)}\big[\xi_x^2 - (G(\eta)\xi)^2 - 2\xi_x\eta_x G(\eta)\xi\big] \end{pmatrix}.$$

The change of variables $\widehat{\mathbf{v}}_k(t) = \Theta(t)\widehat{\mathbf{w}}_k(t)$ in the Fourier space reduces (3.1) to

$$\partial_t \widehat{\mathbf{w}}_k = \Theta(t)^{-1}\widehat{\mathcal{N}}_k\big[\Theta(t)\widehat{\mathbf{w}}_k\big],$$

via the integrating factor

$$\Theta(t) = \begin{pmatrix} \cos\big(t\sqrt{gG_0}\big) & \sqrt{\frac{G_0}{g}}\sin\big(t\sqrt{gG_0}\big) \\ -\sqrt{\frac{g}{G_0}}\sin\big(t\sqrt{gG_0}\big) & \cos\big(t\sqrt{gG_0}\big) \end{pmatrix},$$

for $k \neq 0$, and

$$\Theta(t) = \begin{pmatrix} 1 & 0 \\ -gt & 1 \end{pmatrix}.$$

for $k = 0$. The resulting system only contains nonlinear terms and is solved numerically in time using the fourth-order Runge–Kutta method with constant step Δt. After converting back to $\widehat{\mathbf{v}}_k$, this scheme reads

$$\widehat{\mathbf{v}}_k^{n+1} = \Theta(\Delta t)\widehat{\mathbf{v}}_k^n + \frac{\Delta t}{6}\Theta(\Delta t)\big(f_1 + 2f_2 + 2f_3 + f_4\big),$$

where

$$f_1 = \widehat{\mathcal{N}}_k \left(\widehat{\mathbf{v}}_k^n \right) ,$$

$$f_2 = \Theta \left(-\frac{\Delta t}{2} \right) \widehat{\mathcal{N}}_k \left[\Theta \left(\frac{\Delta t}{2} \right) \left(\widehat{\mathbf{v}}_k^n + \frac{\Delta t}{2} f_1 \right) \right] ,$$

$$f_3 = \Theta \left(-\frac{\Delta t}{2} \right) \widehat{\mathcal{N}}_k \left[\Theta \left(\frac{\Delta t}{2} \right) \left(\widehat{\mathbf{v}}_k^n + \frac{\Delta t}{2} f_2 \right) \right] ,$$

$$f_4 = \Theta(-\Delta t) \widehat{\mathcal{N}}_k \left[\Theta(\Delta t) \left(\widehat{\mathbf{v}}_k^n + \Delta t f_3 \right) \right] ,$$

for the solution at time $t_{n+1} = t_n + \Delta t$.

In cases of large-amplitude or highly deformed waves, filtering is needed in order to stabilize the numerical solution so that it can be computed over a sufficiently long time. Otherwise, spurious high-wavenumber instabilities tend to develop, eventually leading to computation breakdown, unless prohibitively small time steps are specified. This issue may be related to ill-conditioning of the DNO in its series form or may be promoted by the specific nonlinearity of the problem [32]. As a remedy, we apply a hyperviscosity-type filter of the form $\exp(-36|k/k_m|^{36})$ to the Fourier coefficients $\widehat{\eta}_k$ and $\widehat{\xi}_k$ at each time step. Such a filter has been commonly employed in direct numerical simulations of nonlinear fluid flows by spectral methods [27], and its form ensures that only energy levels at high wavenumbers are significantly affected. Therefore, if sufficiently fine resolution is specified, this filtering technique can help suppress spurious instabilities while preserving the overall solution. It also further contributes to removal of aliasing errors and thus blends well into the pseudo-spectral scheme.

4 Applications

In this section, we present applications of our HOS method to wave propagation in a complex environment. Extensions of the mathematical formulation described in Sect. 2 are briefly discussed, and simulations are shown to illustrate the capability and performance of the numerical model. Unless stated otherwise, Eqs. (2.5) and (2.6) are non-dimensionalized such that $g = 1$.

4.1 Fragmented Sea Ice

Floating sea ice is viewed as a thin elastic plate according to the special Cosserat theory of hyperelastic shells [29, 35]. This is modeled by an additional pressure term

of the form $P = F\sigma/\rho$ on the right-hand side of (2.6), where

$$F = \frac{1}{2}\left(\frac{\eta_{xx}}{(1+\eta_x^2)^{3/2}}\right)^3 + \frac{1}{\sqrt{1+\eta_x^2}}\partial_x\left[\frac{1}{\sqrt{1+\eta_x^2}}\partial_x\left(\frac{\eta_{xx}}{(1+\eta_x^2)^{3/2}}\right)\right],$$

with ρ being the fluid density and σ the coefficient of ice rigidity [22, 23]. A spatial distribution of ice floes can be specified in the physical domain by allowing the coefficient of ice rigidity to be a variable function in space, namely $f(x)\sigma/\rho$, whose amplitude varies between 0 (open water) and σ/ρ (pack ice).

To generate a fragmented ice cover of total length L_c, we first prescribe a regular array of N_f identical floes whose individual length is L_f and which are evenly distributed over some distance L_c. Then, to make this arrangement look more irregular (and thus more realistic), each floe is shifted by an amount $\theta L_f/2$ relative to its initial center of gravity, where θ is a random number uniformly distributed between -1 and 1. At the edges of each floe, the continuous transition between the two phases is made steep but smooth enough to clearly distinguish the individual floes while complying with the continuum character of the underlying formulation. We use a tanh-like profile for this phase transition.

Focusing on the shallow-water regime, the present setup features a domain of length $L_m = 1200$, with the ice cover lying between $x = 100$ and $x = 1100$ (hence $L_c = 1000$). The objective is to quantify the attenuation of solitary waves propagating over this distance, for various floe configurations defined by $(N_f, L_f) = (77, 4), (77, 8), (13, 60), (13, 72)$ and corresponding to ice concentrations $C = N_f L_f/L_c = 0.31, 0.62, 0.78, 0.94$ respectively. The numerical parameters are set to $\Delta t = 0.002$, $N = 8192$ and $M = 6$.

Figure 1 shows snapshots of η as a solitary wave of initial amplitude $a_0/h = 0.3$ travels across the ice field. A single realization of each of the floe settings is considered. Two distinct mechanisms contributing to wave attenuation seem to coexist: multiple wave reflections from the ice floes (most apparent in the short-floe configurations), and pulse spreading due to the presence of ice itself (most apparent in the long-floe configurations). For the sparsest floe configuration $(N_f, L_f) = (77, 4)$, the solitary wave is seen to travel essentially unaffected aside from a slight decrease in amplitude. By contrast, for $(N_f, L_f) = (77, 8)$ which has a high level of ice concentration and ice fragmentation, the incident wave quickly decays through backward radiation and pulse spreading.

To further quantify the observed attenuation, Fig. 2 depicts the L^2 norm of η as a function of time for all four floe settings. Motivated by linear predictions [36], the least-squares exponential fit to each data set is also presented as a reference. While the exponential fit performs reasonably well for $(N_f, L_f) = (77, 4)$ when attenuation is weak, it provides a poorer approximation to the numerical data when attenuation is stronger. This is especially apparent in the case $(N_f, L_f) = (77, 8)$ where the data seem to converge to a nonzero limit rather than to zero as time goes on. This behavior may be attributed to the well-known stability of solitary waves
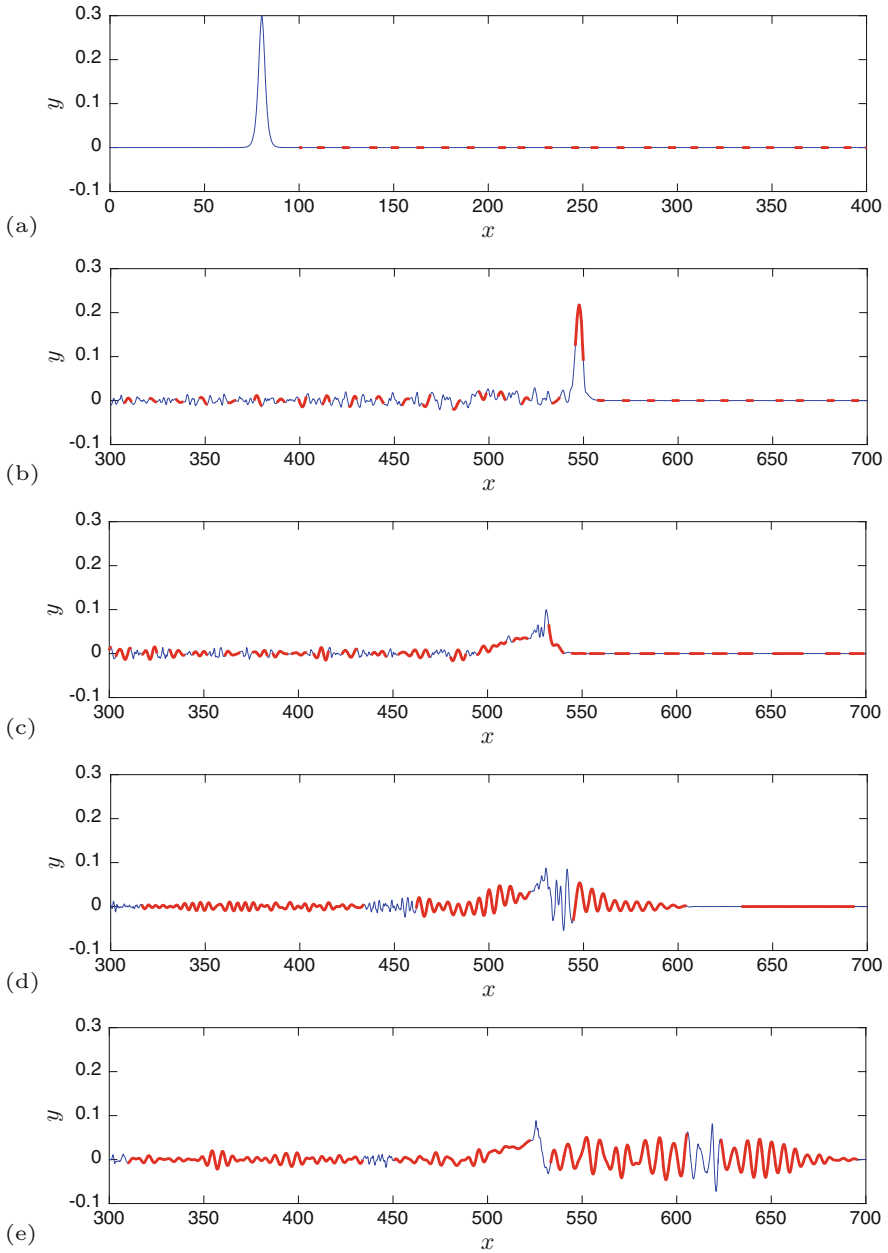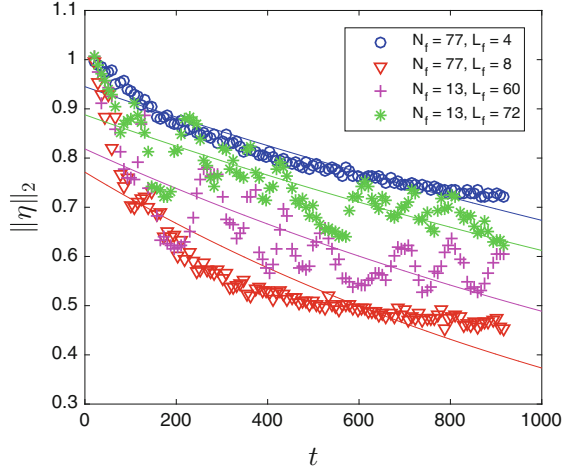
Fig. 1 Snapshots of η for $(N_f, L_f) = (77, 4)$ at $t = 0$ (**a**), $(77, 4)$ at $t = 416$ (**b**), $(77, 8)$ at $t = 416$ (**c**), $(13, 60)$ at $t = 416$ (**d**) and $(13, 72)$ at $t = 416$ (**e**) with $a_0/h = 0.3$. Open water is represented in blue while ice floes are represented in red

Fig. 2 L^2 norm of η as a function of time for $a_0/h = 0.3$. Numerical data are represented in various symbols while their exponential fits are plotted in solid line

[9], which prevents them from completely disintegrating as they travel across the ice field. More details can be found in [24].

4.2 Bottom Topography

In this case, Eqs. (2.5) and (2.6) together with (2.7)–(2.9) can be used verbatim with the only exception that the first term G_0 is replaced by

$$G_0 = D \tanh(hD) + DL(\beta),$$

where $L(\beta)$ takes into account the bottom deformation $\beta(x)$ relative to a reference constant depth h [8, 20]. Because the DNO is jointly analytic with respect to β and η [34], $L(\beta)$ can be expressed in terms of a convergent Taylor series expansion in β,

$$L(\beta) = \sum_{j=0}^{\infty} \operatorname{sech}(hD) L_j(\beta), \tag{4.1}$$

where each L_j can be determined recursively: for even $j > 0$,

$$L_j = - \sum_{\ell=2,\,\text{even}}^{j-2} \frac{\beta^\ell}{\ell!} D^\ell L_{j-\ell} + \sum_{\ell=1,\,\text{odd}}^{j-1} \frac{\beta^\ell}{\ell!} \tanh(hD) D^\ell L_{j-\ell}, \tag{4.2}$$
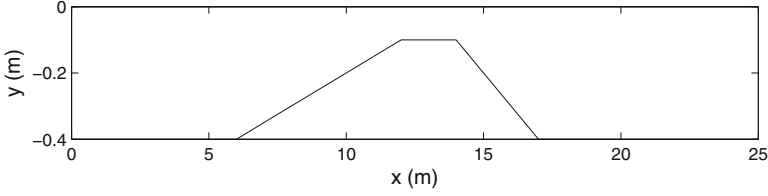
Fig. 3 Submerged bar in the Delft Hydraulics experiments [12]

and, for odd j,

$$
L_j = -\frac{\beta^j}{j!}\mathrm{sech}(hD)D^j - \sum_{\ell=2,\,\text{even}}^{j-1} \frac{\beta^\ell}{\ell!}D^\ell L_{j-\ell} + \sum_{\ell=1,\,\text{odd}}^{j-2} \frac{\beta^\ell}{\ell!}\tanh(hD)D^\ell L_{j-\ell}\,.
$$

(4.3)

These formulas clearly reveal the regularizing character of the DNO with respect to water depth, as indicated by the presence of the smoothing operator $\mathrm{sech}(hD)$. Any non-smoothness in the profile of β would automatically be regularized via action of the DNO, thus producing a C^∞ contribution [2, 10]. Adopting a Fourier series representation for β, Eqs. (4.1)–(4.3) are also evaluated by a pseudo-spectral method with the FFT. Similar to (2.7), the expansion (4.1) is truncated to a finite number of terms M_b that may be selected independently of M.

As an illustration, we consider the Delft Hydraulics bar experiments where a regular Stokes wave breaks up into higher harmonics after passing over a submerged bar [12]. As shown in Fig. 3, the bottom profile is not smooth and its amplitude is comparable to the total water depth. This case is particularly difficult to simulate because it involves wave propagation on deep and shallow water, over a wide range of depths. It has often been used as a discriminating test for nonlinear models of coastal waves. Figure 4 shows time series of η at various locations along the wave channel. At each location, our numerical results are compared with the experimental data. The incident wave has an amplitude $a_0 = 0.02$ m and period $T_0 = 2.02$ s. The numerical parameters are set to $\Delta t = 0.001$ s, $N = 2048$ and $M = M_b = 8$. Overall, the agreement between the two data sets is found to be quite good. In particular, the wave steepening during shoaling ($x < 13.5$ m) and the generation of higher harmonics over the downslope of the bar ($x > 13.5$ m) are well reproduced by the HOS model. More details can be found in [21], including the case of moving bottom topography.
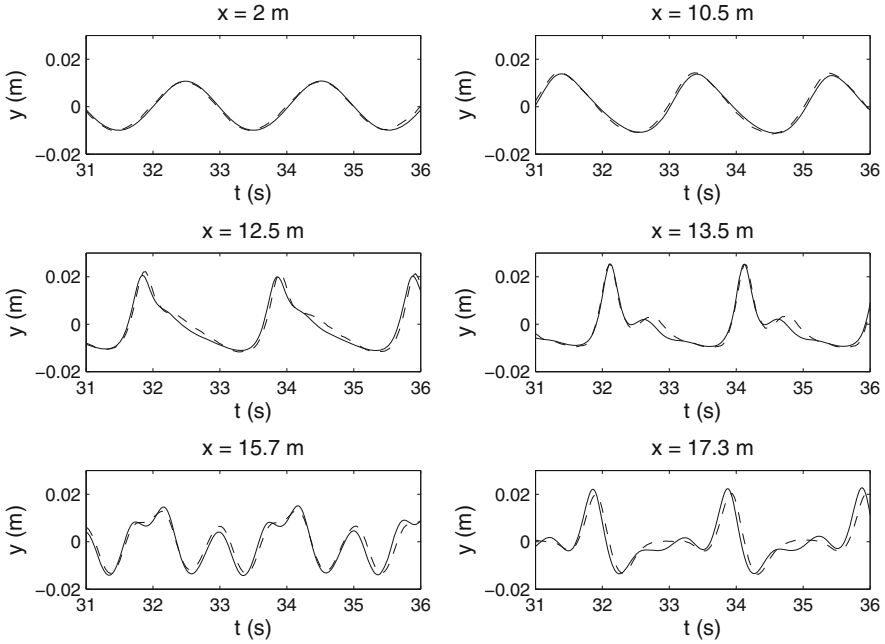
Fig. 4 Time series of η at various locations for an incident Stokes wave with $(a_0, T_0) = (0.02\,\mathrm{m}, 2.02\,\mathrm{s})$ passing over a bar: experiment (dashed line) and simulation (solid line)

4.3 Background Shear Current

In the presence of constant vorticity γ, the rotational flow can be described by two conjugate harmonic functions, namely a velocity potential φ and a stream function ψ, that satisfy

$$\varphi_x = \psi_y = u - U_0 + \gamma y, \qquad \varphi_y = -\psi_x = v,$$

where U_0 denotes a uniform background current [15, 37]. This leads to the following modifications in the Hamiltonian structure of the problem:

$$\begin{pmatrix} \eta_t \\ \xi_t \end{pmatrix} = \begin{pmatrix} 0 & 1 \\ -1 & \gamma \partial_x^{-1} \end{pmatrix} \begin{pmatrix} H_\eta \\ H_\xi \end{pmatrix},$$

with

$$H = \frac{1}{2} \int_{-\infty}^{\infty} \left[\xi G(\eta)\xi - \gamma \xi_x \eta^2 + \frac{1}{3}\gamma^2 \eta^3 - 2U_0 \xi \eta_x + g\eta^2 \right] dx.$$

The corresponding equations of motion take the form

$$\eta_t = G(\eta)\xi - U_0\eta_x + \gamma\eta\eta_x \,,$$

$$\xi_t = -g\eta - \frac{1}{2(1+\eta_x^2)}\Big[\xi_x^2 - (G(\eta)\xi)^2 - 2\xi_x\eta_x G(\eta)\xi\Big] - U_0\xi_x + \gamma\eta\xi_x - \gamma K(\eta)\xi \,,$$

where $K(\eta)\xi$, the Hilbert transform (HT) of ξ, returns the trace of the stream function on the free surface, i.e. $K(\eta)\xi = \psi(x, \eta(x,t), t)$. This is also a nonlocal operator that is related to the DNO by $G(\eta)\xi = -\partial_x K(\eta)\xi$. Similarly, it can be expressed in terms of a Taylor series expansion

$$K(\eta) = \sum_{j=0}^{\infty} K_j(\eta) \,,$$

where

$$K_j = -K_0 D^{j-2}\partial_x \frac{\eta^j}{j!}\partial_x + \sum_{\ell=2,\,\text{even}}^{j} D^{\ell-2}\partial_x \frac{\eta^\ell}{\ell!}\partial_x K_{j-\ell} + \sum_{\ell=1,\,\text{odd}}^{j-1} K_0 D^{\ell-1}\frac{\eta^\ell}{\ell!}\partial_x K_{j-\ell} \,,$$

for even $j > 0$, and

$$K_j = D^{j-1}\frac{\eta^j}{j!}\partial_x + \sum_{\ell=2,\,\text{even}}^{j-1} D^{\ell-2}\partial_x \frac{\eta^\ell}{\ell!}\partial_x K_{j-\ell} + \sum_{\ell=1,\,\text{odd}}^{j} K_0 D^{\ell-1}\frac{\eta^\ell}{\ell!}\partial_x K_{j-\ell} \,,$$

for odd j. The Fourier multiplier $K_0 = \mathrm{i}\tanh(hD)$ represents the HT for a uniform strip of thickness h. Because of this direct relation with the DNO, the same numerical procedure as described in Sect. 3.1 can be used to evaluate the HT series.

For simplicity, the following application only considers the case $U_0 = 0$. We investigate the Benjamin–Feir instability (BFI) of Stokes waves in the presence of a linear shear current. In the irrotational case ($\gamma = 0$), such waves are known to be unstable to sideband perturbations on deep water. We run simulations in a domain of length $L_m = 2\pi$ and infinite depth $h = +\infty$, with initial conditions representing a perturbed Stokes wave. The numerical parameters are set to $\Delta t = 0.001$, $N = 1024$ and $M = 6$. The initial Stokes wave has an amplitude $a_0 = 0.005$ with carrier wavenumber $k_0 = 10$, while the perturbation wavenumber is $\kappa = 1$.

Figure 5 shows snapshots of η at the initial time $t = 0$ for $\gamma = 0$ and at the time of maximum growth for $\gamma = 0, \pm 1, \pm 2$. We find that a co-propagating current ($\gamma > 0$) tends to stabilize the Stokes wave; the larger γ, the stronger the stabilizing effect. For $\gamma = +1$ and $+2$, the BFI seems to be inhibited and the corresponding graphs are not shown here because they look almost identical to Fig. 5a. On the other hand, a counter-propagating current ($\gamma < 0$) tends to promote and enhance the BFI. The larger $|\gamma|$, the sooner the Stokes wave becomes unstable and the higher it grows. For $\gamma = -1$ and -2, the wave reaches an elevation $a_{\max} = 0.016$ and $a_{\max} = 0.025$
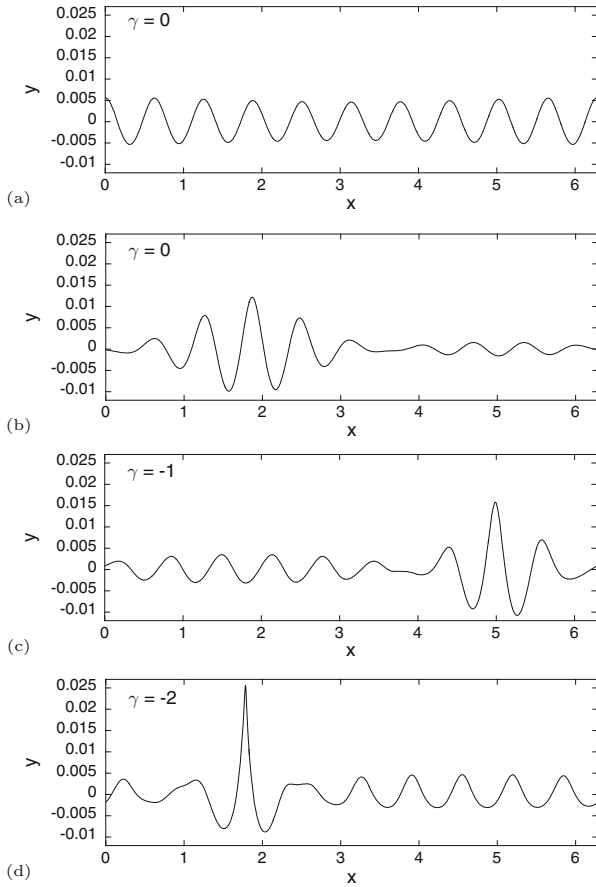
Fig. 5 Snapshots of η at (**a**) $t = 0$ ($\gamma = 0$), (**b**) $t = 956$ ($\gamma = 0$), (**c**) $t = 586$ ($\gamma = -1$) and (**d**) $t = 376$ ($\gamma = -2$) for an initially perturbed Stokes wave with $(a_0, k_0) = (0.005, 10)$ on deep water

at $t = 586$ and $t = 376$ respectively, which corresponds to an amplification factor of $\alpha = 3.2$ and $\alpha = 5$ compared to the initial amplitude a_0. As a reference, the maximum wave growth observed in Fig. 5b for $\gamma = 0$ is $\alpha = 2.4$ ($a_{max} = 0.012$), which agrees with the classical NLS prediction

$$\alpha = \frac{a_{max}}{a_0} = 1 + 2\sqrt{1 - \left(\frac{\kappa}{2\sqrt{2}k_0^2 a_0}\right)^2} = 2.4\,.$$

These results support the fact that wave-current interactions represent a possible mechanism for rogue wave formation in the ocean [15]. More details can be found in [18].

References

1. L. af Klinteberg, A.K. Tornberg, A fast integral equation method for solid particles in viscous flow using quadrature by expansion. J. Comput. Phys. **326**, 420–445 (2016)
2. M. Cathala, Asymptotic shallow water models with non smooth topographies. Monatsh. Math. **179**, 325–353 (2016)
3. R. Coifman, Y. Meyer, Nonlinear harmonic analysis and analytic dependence. Proc. Symp. Pure Math. **43**, 71–78 (1985)
4. A. Compelli, Hamiltonian formulation of 2 bounded immiscible media with constant non-zero vorticities and a common interface. Wave Motion **54**, 115–124 (2015)
5. W. Craig, D.P. Nicholls, Traveling gravity water waves in two and three dimensions. Eur. J. Mech. B/Fluids **21**, 615–641 (2002)
6. W. Craig, C. Sulem, Numerical simulation of gravity waves. J. Comput. Phys. **108**, 73–83 (1993)
7. W. Craig, P. Guyenne, H. Kalisch, Hamiltonian long wave expansions for free surfaces and interfaces. Commun. Pure Appl. Math. **58**, 1587–1641 (2005)
8. W. Craig, P. Guyenne, D.P. Nicholls, C. Sulem, Hamiltonian long-wave expansions for water waves over a rough bottom. Proc. R. Soc. A **461**, 839–873 (2005)
9. W. Craig, P. Guyenne, J. Hammack, D. Henderson, C. Sulem, Solitary water wave interactions. Phys. Fluids **18**, 057106 (2006)
10. W. Craig, P. Guyenne, C. Sulem, Water waves over a random bottom. J. Fluid Mech. **640**, 79–107 (2009)
11. W. Craig, P. Guyenne, C. Sulem, Internal waves coupled to surface gravity waves in three dimensions. Commun. Math. Sci. **13**, 893–910 (2015)
12. M.W. Dingemans, Comparison of computations with Boussinesq-like models and laboratory measurements, in *Technical Report H1684.12* (Delft Hydraulics, Delft, 1994)
13. D.G. Dommermuth, D.K.P. Yue, A high-order spectral method for the study of nonlinear gravity waves. J. Fluid Mech. **184**, 267–288 (1987)
14. G. Ducrozet, F. Bonnefoy, D. Le Touzé, P. Ferrant, HOS-ocean: open-source solver for nonlinear waves in open ocean based on high-order spectral method. Comput. Phys. Commun. **203**, 245–254 (2016)
15. M. Francius, C. Kharif, S. Viroulet,Nonlinear simulations of surface waves in finite depth on a linear shear current, in *Proceedings of the 7th International Conference on Coastal Dynamics* (2013), pp. 649–660.
16. L. Greengard, V. Rokhlin, A fast algorithm for particle simulations. J. Comput. Phys. **73**, 325–348 (1987)
17. S.T. Grilli, P. Guyenne, F. Dias, A fully nonlinear model for three-dimensional overturning waves over an arbitrary bottom. Int. J. Numer. Meth. Fluids **35**, 829–867 (2001)
18. P. Guyenne, A high-order spectral method for nonlinear water waves in the presence of a linear shear current. Comput. Fluids **154**, 224–235 (2017)
19. P. Guyenne, S.T. Grilli, Numerical study of three-dimensional overturning waves in shallow water. J. Fluid Mech. **547**, 361–388 (2006)
20. P. Guyenne, D.P. Nicholls, Numerical simulation of solitary waves on plane slopes. Math. Comput. Simul. **69**, 269–281 (2005)
21. P. Guyenne, D.P. Nicholls, A high-order spectral method for nonlinear water waves over moving bottom topography. SIAM J. Sci. Comput. **30**, 81–101 (2007)

22. P. Guyenne, E.I. Părău, Computations of fully nonlinear hydroelastic solitary waves on deep water. J. Fluid Mech. **713**, 307–329 (2012)

23. P. Guyenne, E.I. Părău, Finite-depth effects on solitary waves in a floating ice sheet. J. Fluids Struct. **49**, 242–262 (2014)

24. P. Guyenne, E.I. Părău, Numerical study of solitary wave attenuation in a fragmented ice sheet. Phys. Rev. Fluids **2**, 034002 (2017)

25. P. Guyenne, D. Lannes, J.-C. Saut, Well-posedness of the Cauchy problem for models of large amplitude internal waves. Nonlinearity **23**, 237–275 (2010)

26. N. Hale, A. Townsend, A fast, simple, and stable Chebyshev–Legendre transform using an asymptotic formula. SIAM J. Sci. Comput. **36**, A148–A167 (2014)

27. T.Y. Hou, J.S. Lowengrub, M.J. Shelley, Removing the stiffness from interfacial flows with surface tension. J. Comput. Phys. **114**, 312–338 (1994)

28. Y. Liu, D.K.P. Yue, On generalized Bragg scattering of surface waves by bottom ripples. J. Fluid Mech. **356**, 297–326 (1998)

29. P.A. Milewski, Z. Wang, Three dimensional flexural-gravity waves. Stud. Appl. Math. **131**, 135–148 (2013)

30. D.P. Nicholls, Traveling water waves: spectral continuation methods with parallel implementation. J. Comput. Phys. **143**, 224–240 (1998)

31. D.P. Nicholls, Boundary perturbation methods for water waves. GAMM-Mitt. **30**, 44–74 (2007)

32. D.P. Nicholls, F. Reitich, Stability of high-order perturbative methods for the computation of Dirichlet–Neumann operators. J. Comput. Phys. **170**, 276–298 (2001)

33. D.P. Nicholls, F. Reitich, A new approach to analyticity of Dirichlet–Neumann operators. Proc. Roy. Soc. Edinburgh Sect. A **131**, 1411–1433 (2001)

34. D.P. Nicholls, M. Taber, Joint analyticity and analytic continuation of Dirichlet–Neumann operators on doubly perturbed domains. J. Math. Fluid Mech. **10**, 238–271 (2008)

35. P.I. Plotnikov, J.F. Toland, Modelling nonlinear hydroelastic waves. Phil. Trans. R. Soc. Lond. A **369**, 2942–2956 (2011)

36. P. Wadhams, V.A. Squire, D.J. Goodman, A.M. Cowan, S.C. Moore, The attenuation rates of ocean waves in the marginal ice zone. J. Geophys. Res. **93**, 6799–6818 (1988)

37. E. Wahlén, A Hamiltonian formulation of water waves with constant vorticity. Lett. Math. Phys. **79**, 303–315 (2007)

38. B.J. West, K.A. Brueckner, R.S. Janda, D.M. Milder, R.L. Milton, A new numerical method for surface hydrodynamics. J. Geophys. Res. **92**, 11803–11824 (1987)

39. L. Xu, P. Guyenne, Numerical simulation of three-dimensional nonlinear water waves. J. Comput. Phys. **228**, 8446–8466 (2009)

40. V.E. Zakharov, Stability of periodic waves of finite amplitude on the surface of a deep fluid. J. Appl. Mech. Tech. Phys. **9**, 190–194 (1968)